International Journal of Minerals, Metallurgy and Materials
Volume 26, Number 9, September 2019, Page 1151
https://doi.org/10.1007/s12613-019-1854-1

New high-strength Ti–Al–V–Mo alloy: from high-throughput composition design to mechanical properties

Di Wu[1,2], *Wan-lin Wang*[1], *Li-gang Zhang*[2,3], *Zhen-yu Wang*[2], *Ke-chao Zhou*[4], *and Li-bin Liu*[2,3]

1) School of Metallurgy and Environment, Central South University, Changsha 410083, China
2) School of Material Science and Engineering, Central South University, Changsha 410083, China
3) Key Laboratory of Non-Ferrous Metallic Materials Science and Engineering, Ministry of Education, Changsha 410083, China
4) State Key Laboratory of Powder Metallurgy, Changsha 410083, China
(Received: 13 January 2019; revised: 22 February 2019; accepted: 27 February 201)

Abstract: The high-throughput diffusion-multiple technique and thermodynamics databases were used to design new high-strength Ti alloys. The composition–microstructure–property relationships of the Ti64–*x*Mo alloys were obtained. The phase fraction and composition of the α and β phases of the Ti64–*x*Mo alloys were calculated using the Thermo-Calc software. After aging at 600°C, the Ti64–6Mo alloy precipitated ultrafine α phases. This phenomenon was explained on the basis of the pseudo-spinodal mechanism by calculating the Gibbs energy curves of the α and β phases of the Ti64–*x*Mo alloys at 600°C. Bulk forged Ti64–6Mo alloy exhibited high strength and moderate plasticity after α/β-phase-field solution treatment plus aging. The tensile properties of the alloy were determined by the size and morphology of the primary and secondary α phases and by the β grain size.

Keywords: high-strength titanium alloy; Ti–6Al–4V–*x*Mo; diffusion multiple; Thermo-Calc; microstructure and mechanical properties

1. Introduction

Ti64 (Ti−6Al−4V) alloy has a wide range of applications in the aerospace industry because of its excellent comprehensive performance [1–6]. It is mainly used to manufacture fan air-pressure disks and blades for engines and structural components such as beams, joints, and bulkheads [7–9]. As an α+β two-phase alloy, Ti64 alloy exhibits a strength of approximately 900 MPa after thermomechanical processing; this low strength continues to limit the applications of the alloy. High-strength Ti alloys widely used in the aircraft industry include Ti–10V–2Fe–3Al [10–11], Ti−5Al−5Mo–5V−1Cr [12], the new Ti−5Al−5Mo–5V−3Cr−1Zr [13–14], and Ti−7Mo–3Al−3Cr−3Nb [15] alloys. In general, these high-strength Ti alloys are metastable β or near-β Ti alloys, with a strength of 1300 MPa after a solution and aging treatment. Adding β stabilizers to change the α+β-type Ti alloy to a β or near-β Ti alloy is an effective method to enhance the strength. In addition, the microstructure of the alloy can be controlled through subsequent thermal processing and heat treatment, which can improve the elongation and fracture toughness of the alloy.

Mo is an effective isomorphous β-stabilizing element that is widely used in various high-strength Ti alloys. Examples of alloys with Mo are Ti–15Mo–2.6Nb–3Al–0.2Si [16], Ti–5Mo–5A1–5V–3Cr [17–18], and Ti–7Mo–3Al–3Cr–3Nb [19]. Mo can be dissolved in Ti alloys infinitely and can effectively strengthen the alloy without forming harmful brittle intermetallic compounds that reduce material ductility and toughness. Mo is also widely used in various types of Ti alloys [20–25]. Therefore, Mo can be used to modify Ti64 alloy.

Traditional methods of alloy design require casting, homogenization, hot working, and heat treatment, which are costly and time consuming. The diffusion-multiple approach has been successfully used to determine the isothermal section of the ternary phase diagram. Zhao *and* other researchers [26–29] extended the application range of the diffusion-multiple approach and studied the microstructure and properties of alloys with different compositions. Through

Corresponding authors: Ke-chao Zhou E-mail: zhoukechao@csu.edu.cn; Li-bin Liu E-mail: lbliu@csu.edu.cn

this approach, a "composition–microstructure–properties" database for an alloy can be rapidly obtained for one sample and then used to design new alloys. Zhang *et al*. [30] used this method to study the effects of different Zr and Ta concentrations on the hardness and elastic modulus of Ti alloys. Wu *et al*. [31] investigated the influence of Cr content on the microstructure and hardness of Ti−6Al–4V alloys. Therefore, we used a combinatorial diffusion-multiple approach in the present research.

In this work, we studied the effect of Mo content on the microstructure and properties of Ti64 alloy and designed a new type of high-strength Ti64−6Mo alloy through the diffusion-multiple approach and CALPHAD thermodynamic calculations. The bulk alloy was manufactured, and its microstructure and tensile properties were investigated. The results show that the designed alloy displayed excellent comprehensive properties, indicating that the combinatorial approach is an effective tool for designing new alloys.

2. Experimental

The diffusion multiples are composed of several diffusion couples and diffusion triplets arranged in a specific combination [27,32]. The preparation process of the Ti6Al4V−Ti6Al4V45Zr−Ti6Al4V20Mo−Ti6Al4V20Fe−Ti6Al4V20Cr diffusion multiple is shown in Fig. 1. The alloys used to prepare the diffusion multiple were smelted three times using a vacuum arc furnace. The alloy was machined into the desired shape via electrical discharge machining. The alloys used in the experiment include two pieces of Ti64 alloy with dimensions of 10 mm × 12 mm × 12 mm; two pieces of Ti64−45Zr; one piece each of Ti64−20Mo and Ti64−20Cr alloys with dimensions of 3 mm × 12 mm × 12 mm; and one piece each of Ti64−20Mo, Ti64−20Fe, and Ti64−20Cr alloys with dimensions of 3 mm × 12 mm × 16 mm. The Ti64 and Ti64−20Mo alloys were obtained by melting high-purity Ti (99.95%), Mo (99.95%), V (99.95%), and Al (99.99%) in an electric arc furnace. The chemical composition of the Ti64 and Ti64−20Mo alloys is shown in Table 1.

As shown in Fig. 1(a), the two sandwich ternary diffusion couples namely, Ti6Al4V–Ti6Al4V45Zr–Ti6Al4V20Mo and Ti6Al4V–Ti6Al4V45Zr–Ti6Al4V20Cr—were manufactured using a steel fixture after the alloy samples were ground and polished. Diffusion welding was carried out under vacuum (~10^{-3} Pa) at 1000°C for 4 h. The steel fixture and alloys were separated by a Ta foil to prevent diffusion. After the Ti6Al4V–Ti6Al4V45Zr–Ti6Al4V20Mo and Ti6Al4V–Ti6Al4V45Zr–Ti6Al4V20Cr samples were removed from the fixture, the surface was polished, and the Ti6Al4V−Ti6Al4V45Zr−Ti6Al4V20Mo−Ti6Al4V20Fe−Ti6Al4V20Cr diffusion multiple was manufactured using a steel fixture again, as shown in Fig. 1(b). The diffusion multiple was diffusion annealed at 1100°C for 240 h in an evacuated quartz tube. The sample was solution treated at 1050°C for 6 h, water-cooled, aged at 600°C for 6 h, and then air-cooled. The heat-treatment schedule of the diffusion multiple is shown in Fig. 2.

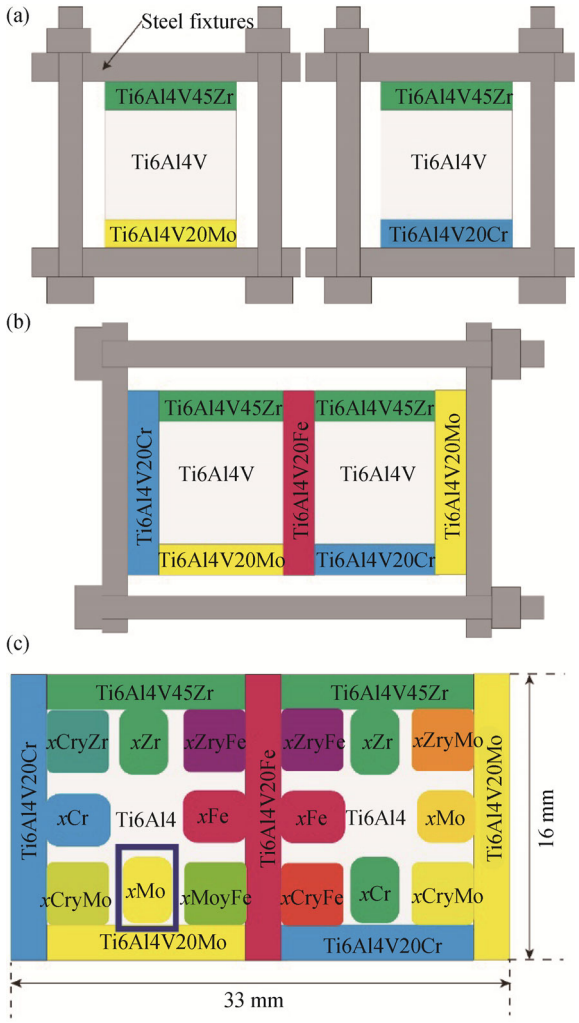

Fig. 1. Preparation process of diffusion multiple Ti6Al4V−Ti6Al4V45Zr−Ti6Al4V20Mo−Ti6Al4V20Fe−Ti6Al4V20Cr: (a) preparation of two sandwich diffusion couples with steel fixtures; (b) preparation of the diffusion multiple using a steel fixture; (c) cross-sectional schematics of the diffusion multiple.

Table 1. Chemical composition of the Ti6Al4V and Ti6Al4V20Mo alloys wt%

Alloy	Al	V	Mo	O	N	C	Ti
Ti6Al4V	6.37	3.61	—	0.18	0.02	0.02	Bal.
Ti6Al4V20Mo	6.16	3.82	22.16	0.09	0.016	0.011	Bal.

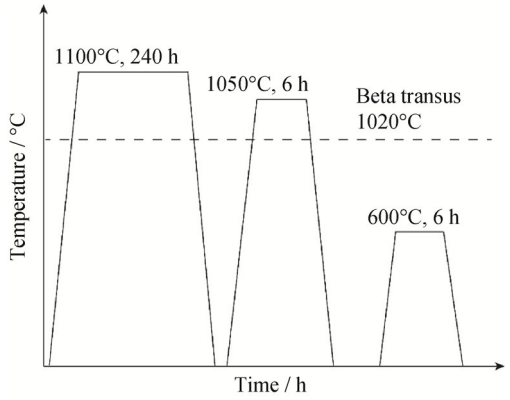

Fig. 2. Heat-treatment flow chart for the Ti6Al4V−Ti6Al4V45Zr−Ti6Al4V20Mo−Ti6Al4V20Fe−Ti6Al4V20Cr diffusion multiple.

After the oxide layer was removed from the sample, it was sanded with 400#, 600#, 800#, and 1000# sandpaper, mechanically polished for ~15 min, ultrasonically cleaned with ethanol, and dried. Electron-probe microanalysis (EPMA) was used to determine the element distribution of the diffusion multiple. A microhardness tester was subsequently used to determine the hardness in the diffusion region. The electron probe was then used to detect the alloy compositions near the indentation points. Afterwards, the microstructure of the alloys near the indentation points was observed by scanning electron microscopy (SEM). The composition of the alloy was measured on a JEOL JXA-8230 microprobe with parameters of a 40° take-off angle, accelerating voltage of 15 kV, and accelerating current of 20 nA. The microhardness measurements were carried out on a BUEHLER 5104 microhardness system with an indentation load of 500 mN and a holding time of 15 s. Microstructure analysis was performed on a NOVATM Nano SEM 230 field-emission scanning electron microscope operated at an acceleration voltage of 20 kV and operating distance of 5 mm. A button ingot (~10 g) of Ti64−6Mo was prepared from high-purity Ti, Al, V, and Mo. The alloy ingot was obtained after three melting sequences in a non-consumable vacuum arc furnace and was subjected to a similar heat treatment as the diffusion-couple sample. The phase morphology and phase composition were characterized on a Titan G260-300 spherical aberration correction field-emission transmission electron microscope.

The bulk Ti64−6Mo alloy was made of Ti sponge, pure Al, Al–V, and Ti–Mo intermediate alloy. A vacuum consumable arc was used to melt the alloy ingot with a mass of 20 kg and diameter of 160 mm. The alloy ingot was first forged at 1050°C (β single-phase field) and then forged at 850°C (α + β two-phase field) into a square rod with approximate dimensions of 1000 mm × 80 mm × 40 mm. The forged Ti64−6Mo alloy was solution treated at 825 and 900°C for 0.5 h and then air-cooled. Thereafter, the aging treatment was carried out at 520, 560, 600, or 640°C for 6 h. Tensile testing was then carried out on the MTS 810 tensile test system. The uniform portion of the tensile specimen was 25 mm × 4 mm × 3 mm, and the stretching speed was 2 mm/min.

In conjunction with the thermodynamic database for the Ti–Al–Mo–V system, the Thermo-Calc software was used to calculate the following: (1) the phase-fraction and free-energy curves of the α and β phases of Ti64–*x*Mo alloys at 600°C; (2) the phase composition of the Ti64–6Mo alloys at 600°C.

3. Results

3.1. Scanning electron microscopy analysis of Ti64–*x*Mo alloy

Fig. 3 shows an optical micrograph and composition distribution curve of Ti6Al4V–Ti6Al4V20Mo diffusion couple after diffusion annealing and quenching from the β-phase region. As shown in Fig. 3(a), the microhardness indentation was uniformly distributed in the diffusion region to obtain a series of hardness data, and EPMA was used to determine the alloy composition near the indentation. Fig. 3(b) is the composition–distance curve for the Ti6Al4V–Ti6Al4V20Mo diffusion couple. The Mo atoms diffused into the Ti64, where they mainly replaced Ti atoms.

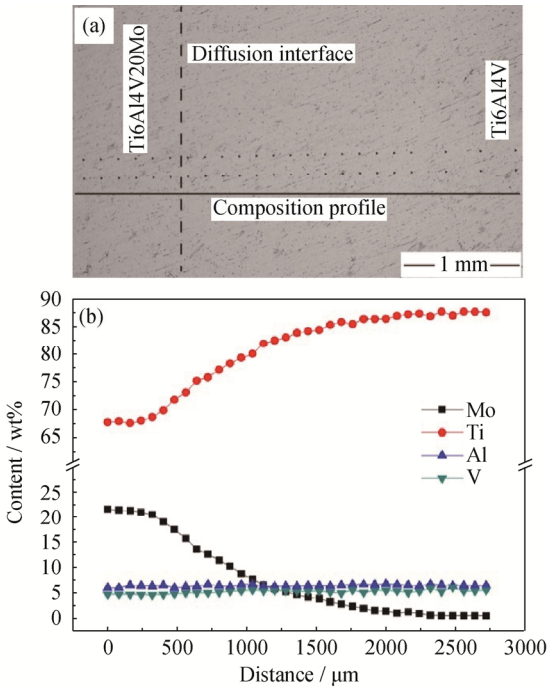

Fig. 3. Optical image of the Ti6Al4V–Ti6Al4V20Mo diffusion-coupling interface with a hardness indentation lattice (a) and element distribution at the diffusion-couple interface (b).

Fig. 4 shows the backscattered-electron images of the Ti6Al4V–Ti6Al4V20Mo diffusion multiple at different positions, with an approximate composition of Ti64–*x*Mo ($x \approx$ 1, 2, 3…). As shown in Figs. 4(a) and 4(b), the quenched Ti64 and Ti64–1Mo are composed of coarse lath martensite α′ and β matrices, and the volume fraction of the martensite α′ phase is very high. As the Mo content is increased to 2wt%–4wt%, the martensite α′ lath becomes thin and the volume fraction decreases. When the Mo content is increases to 5wt%, the fine needle-like martensite α′ and a large amount of metastable β phase are observed. When the Mo content reaches 6wt% or greater, only the β phase is observed. The martensite α′ phase transition is suppressed and the β phase is completely retained during rapid cooling. The formation of martensite in Ti alloys is a shear-type phase transition [33–34]. During quenching, the atoms in the alloy undergo rapid shear displacement. The atomic displacement is large when the β-stabilizer content is low, resulting in formation of the hexagonal α′ phase. However, as the β-stabilizer increases, the driving force for martensite formation decreases, resulting in the formation of a single β phase. Moreover, similar results were obtained for other types of Ti alloys, such as in Ti–10Zr–*x*Mo [35] and Ti–5Cr–*x*Mo [36].

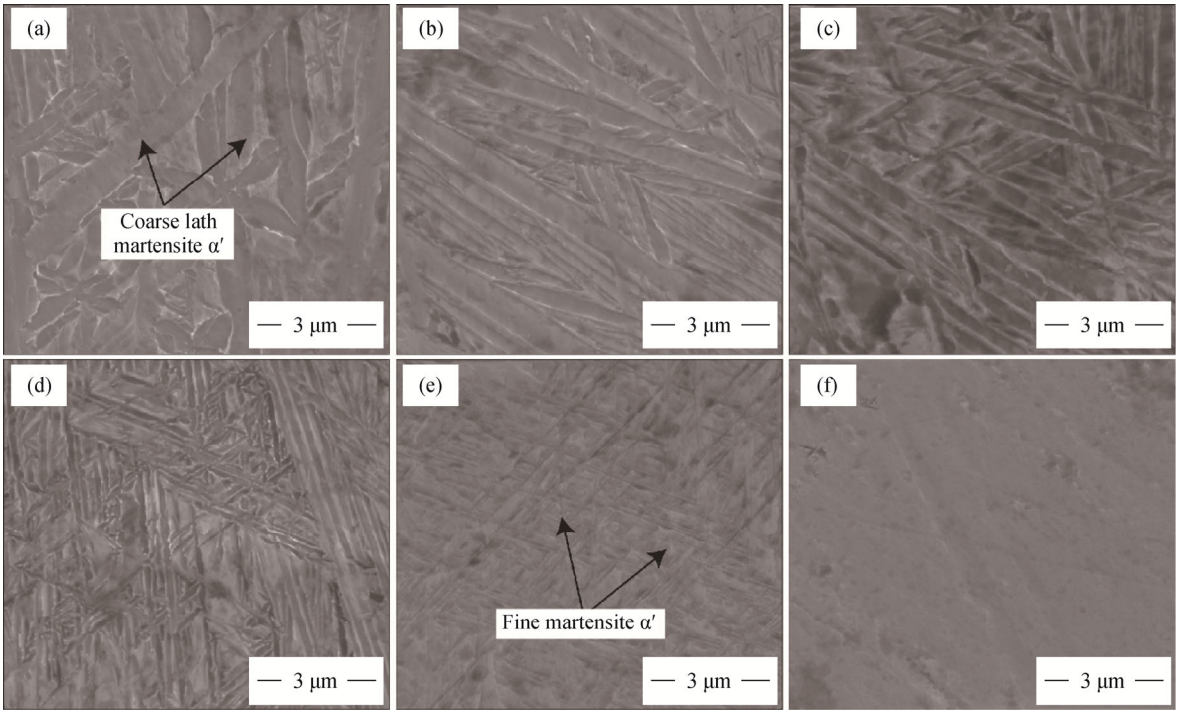

Fig. 4. Backscattered-electron images of quenched Ti64–*x*Mo alloys obtained from a Ti6Al4V–Ti6Al4V20Mo diffusion couple: (a) Ti6Al4V; (b) Ti6Al4V1Mo; (c) Ti6Al4V2Mo; (d) Ti6Al4V4Mo; (e) Ti6Al4V5Mo; (f) Ti6Al4V6Mo.

The backscattering images of a series of aged Ti64–*x*Mo alloys taken from the Ti6Al4V–Ti6Al4V20Mo diffusion couple are shown in Fig. 5. The Ti64 and Ti64–1Mo alloys consist of coarse α phase and the volume fraction of α phase is high (Figs. 5(a) and 5(b)). When the Mo content increases to 2wt%–5wt%, the α lath becomes thin and the volume fraction of the α phase decreases. When the Mo content reaches 6wt%, the Ti64–6Mo alloy has the finest α-phase lath, which is hardly distinguishable by SEM observation. When the Mo content reaches 8wt% or greater, the α phase becomes coarse and the α phase volume fraction further decreases.

The quantitative statistics of the volume fraction of the α phase in the series of Ti64−*x*Mo alloy is shown in Fig. 6(a). As the Mo content increases from 0 to 15wt%, the α-phase volume fraction decreases from 87% to 23%. In conjunction with the thermodynamic database for the Ti–Al–V–Mo system, Thermo-Calc was used to calculate the α-phase fraction of the series of Ti64–*x*Mo alloys at 600°C. The calculation results are in good agreement with the experimental results. As a strong β-stabilizing element, Mo suppresses the formation of the α phase, whose volume fraction decreases. The quantitative statistical results for the thickness of the α phase in Ti64–*x*Mo alloys are shown in Fig. 6(b). When the Mo content is increased from 0 to 6wt%, the thickness of the α phase decreases from 1200 nm to 50 nm and the thickness of the α phase gradually increases to 453 nm as the Mo content is increased to 15wt%. When the Mo content is 0–5wt%, the martensite transformation temperature is

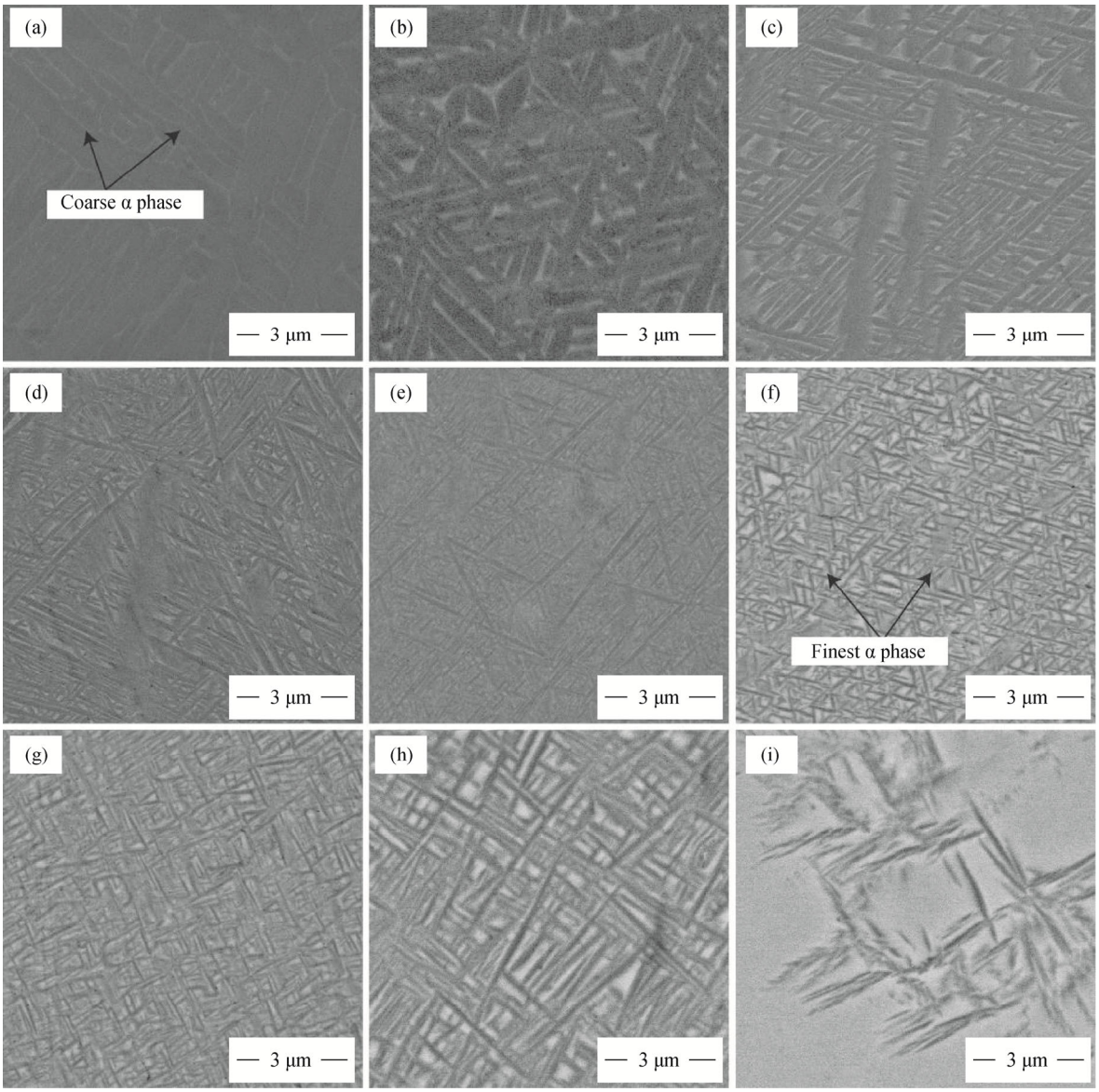

Fig. 5. Backscattered-electron images of aged (600°C for 6 h) Ti64–*x*Mo alloys obtained from the Ti6Al4V–Ti6Al4V20Mo diffusion couple: (a) Ti6Al4V; (b) Ti6Al4V1Mo; (c) Ti6Al4V2Mo; (d) Ti6Al4V4Mo; (e) Ti6Al4V5Mo; (f) Ti6Al4V6Mo; (g) Ti6Al4V8Mo; (h) Ti6Al4V11Mo; (i) Ti6Al4V15Mo.

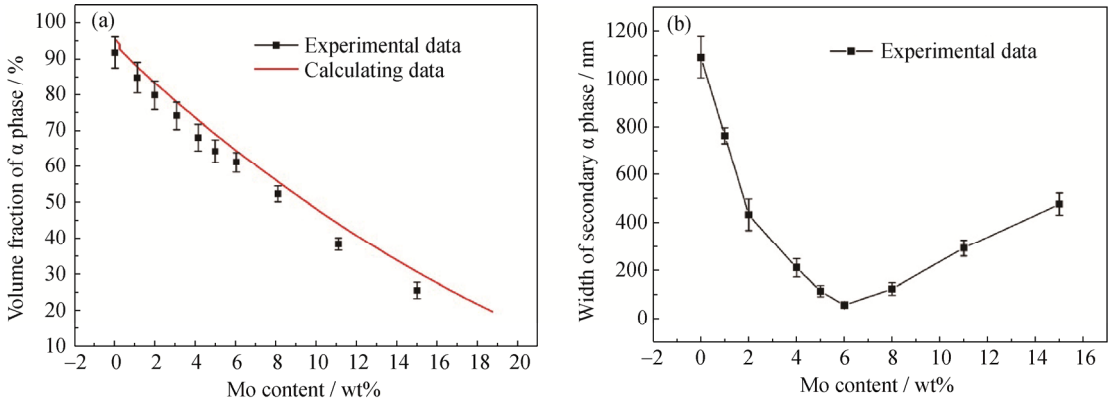

Fig. 6. Volume fraction of the α phase (calculation and experimental results) varies with the Mo content in the sample aged at 600°C (a) and the width of the α phase varies with the Mo content in the sample aged at 600°C (b).

greater than room temperature. During quenching, martensite α′ is formed, and the morphology of the α phase depends largely on quenching martensite α′. Afterwards, the α′-to-α transition occurs upon diffusion of Al, Mo, and V atoms during aging. When the alloy contains 6wt% Mo, the quenched Ti64–6Mo alloy presents a single β phase and the aged alloy shows the morphology of the finest α precipitates. This phase-transition mechanism will be discussed in greater depth in section 4.1.

3.2. Hardness of series Ti64–*x*Mo alloys

Fig. 7 shows the relation between the Mo content and the corresponding alloy hardness and diffusion distance in the Ti6Al4V–Ti6Al4V20Mo diffusion couple. In the as-quenched condition, the hardness of the alloy increases from 411 MPa to 508 MPa when the Mo content increases from 0 to 5wt%, and the alloy hardness decreases to 390 MPa rapidly as the Mo content increases to 7wt%. Finally, as the Mo content continues to increase, the hardness of the alloy gradually increases. In the aged condition, when the Mo content increases from 0 to 6wt%, the hardness of the alloy increases from 431 MPa to 597 MPa; after the hardness of the alloy reaches a maximum, it then decreases with increasing Mo content.

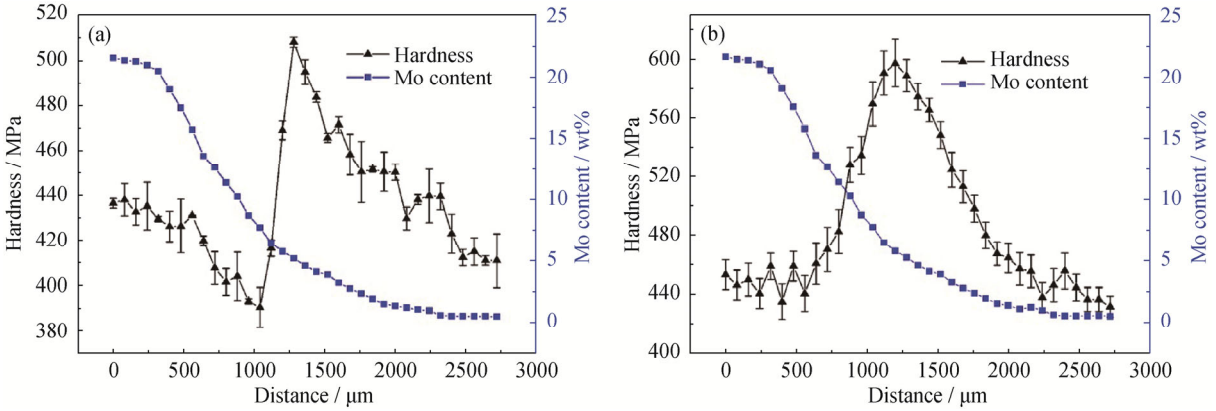

Fig. 7. "Composition–hardness–diffusion distance" curve of the Ti6Al4V–Ti6Al4V20Mo diffusion couple: (a) after quenching from the β-phase region; (b) after aging at 600°C.

3.3. Scanning transmission electron microscopy (STEM) analysis of Ti64–6Mo alloy

Fig. 8 shows the results of the STEM micromorphology analysis of the Ti64–6Mo alloy after solution treatment in the β-phase region. As shown in Figs. 8(a) and 8(b), the bright-field picture and the selected-area electron diffraction results show that the quenched alloy is a single β phase. No evidence suggests that the alloy contains other phases, such as the ω and α″ phases. The distribution of alloying elements after quenching in the β single-phase region was obtained using energy-dispersive spectroscopy (EDS) mapping; the results are shown in Figs. 8(c)–8(d). All of the alloying elements of Mo, V, and Al were uniformly distributed in the β matrix.

The microstructure of Ti64–6Mo alloy after aging at 600°C for 6 h is shown in Fig. 9. Fig. 9(a) shows a bright-field image with a nanosized α phase uniformly distributed within the beta grains. The diffraction spots along the [111] β-ribbon axis direction are shown in Fig. 9(b), wherein the alloy consists of β and α phases. Fig. 9(c) shows a STEM image in high-angle annular dark field (HAADF) mode. The nanosized α phase is clearly visible and evenly distributed on the β matrix. In the aging state, the α phase is approximately 150 nm in length and 50 nm in width. The EDS component scan was performed in the green square area in Fig. 9(d). The distribution of alloying elements in the aged state is shown in Fig. 9(e). The elements such as Al, V, and Mo have distinct color differences between the β and α phases, and the composition distribution curves of quantitative statistics are shown in Fig. 9(f). The quantitative statistics of the chemical components of the α and β phases are shown in Table 1, wherein the Al atoms are mainly enriched in the α phase, and the V and Mo atoms are enriched in the β phase. The mass fractions in the β phase are 4.1wt%, 9.6wt%, and 12.5wt%, respectively, and the components in the α phase are 6.6wt%, 0.44wt%, and 1.48wt%, respectively. In conjunction with the thermodynamic database for Ti alloys, the Thermo-Calc software was used to calculate the phase composition of the α/β phase; the calculation results are consistent with the experimental results (Table 2).

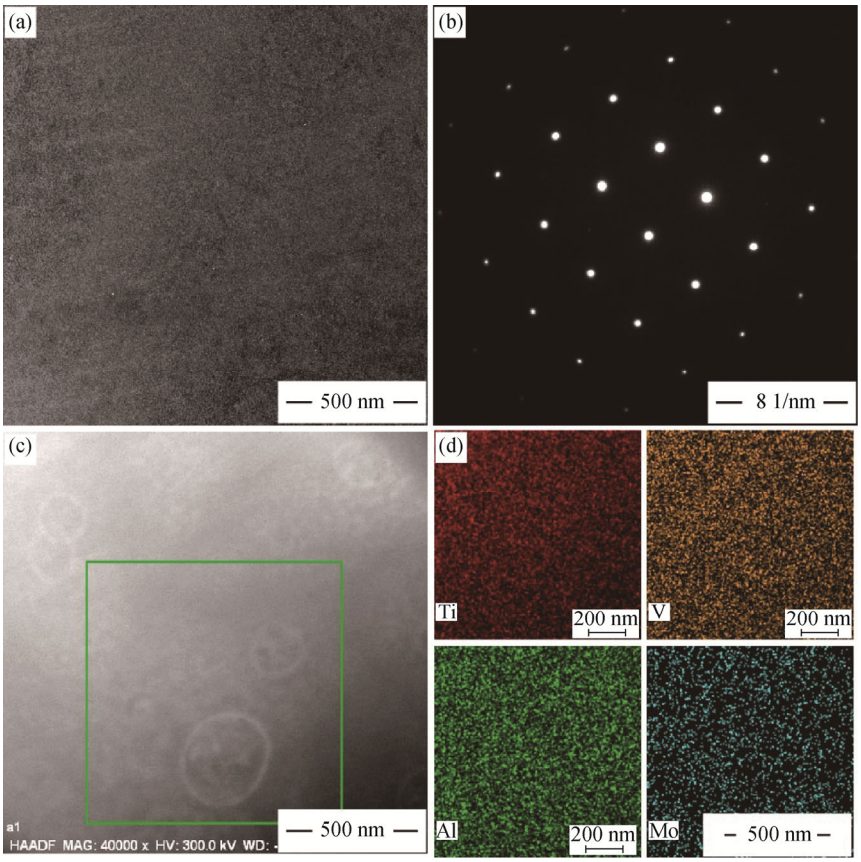

Fig. 8. Microscopic analysis of the Ti64–6Mo alloy after quenching from β phase region: (a) bright-field morphology; (b) SAD pattern with [111] β zone axis; (c) HAADF–STEM images; (d) EDS composition mapping of Ti, Al, V, and Mo atoms.

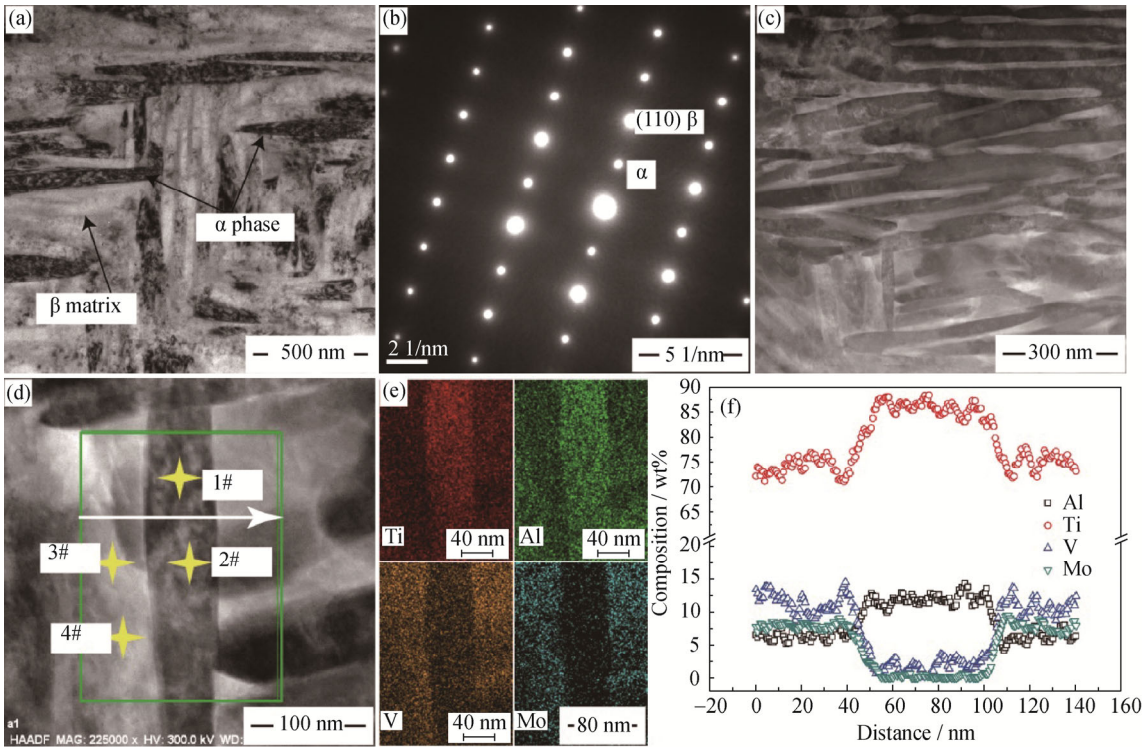

Fig. 9. Microscopic analysis of the Ti64–6Mo alloy after aging at 600°C: (a) bright-field morphology; (b) SAED pattern with [111] β zone axis; (c and d) HAADF–STEM images showing the α phase; (e) the EDS mapping of Mo, V, Al, and Ti atoms; (f) the composition profiles along the arrows shown in (d).

Table 2. Experimental and calculated alloying elements in the α and β phases of Ti64–6Mo alloy aged at 600°C wt%

Position in Fig. 9(d)	Phase	V	Mo	Ti	Al
1	α	1.54	0.23	90.9	6.7
2	α	1.41	0.64	91.4	6.5
3	β	9.3	12.1	74.4	4.2
4	β	9.9	12.8	73.1	4.0
Calculation data	α	1.8	0.26	91.7	6.7
	β	10.1	21.9	63.5	4.3

3.4. Microstructure and tensile properties of the forged Ti64–6Mo alloy

Inductively coupled plasma atomic emission spectrometry method was used to test the actual composition of the forged ingot. The test results are shown in Table 3. The α/β transition temperature of the forged Ti64–6Mo alloy was tested using the metallographic method, which was about 875°C. Fig. 10(a) is the initial microscopic morphology of the forged Ti64–6Mo alloy. A large number of gray α phases appear on the β matrix. The X-ray diffraction (XRD) results for the forged state of the Ti64–6Mo alloy are shown in Fig. 10(b), which confirms of the existence of α and β two phases in the alloy. The SEM microstructure of the Ti64–6Mo alloy after solution treatment at 825°C and 900°C is shown in Figs. 10(c) and 10(d). The alloy solution treated at 825°C consists of equiaxed spherical α phase and a β matrix with a β grain size of approximately 5 μm. These spherical α phases are called primary α phases, and they preferentially nucleate at the β grain boundary. These α phases located at the β grain boundary can effectively prevent the migration of the β grain boundary and inhibit β grain growth during solution treatment. When the alloy is solution treated in the β single-phase region, the alloy consists of large β grains with a grain size of 20 μm.

Table 3. Chemical composition of the Ti–6Al–6Mo–4V alloy wt%

Al	Mo	V	Fe	Si	C	O	N	Ti
5.63	5.91	4.45	0.045	0.271	0.023	0.183	0.009	Bal.

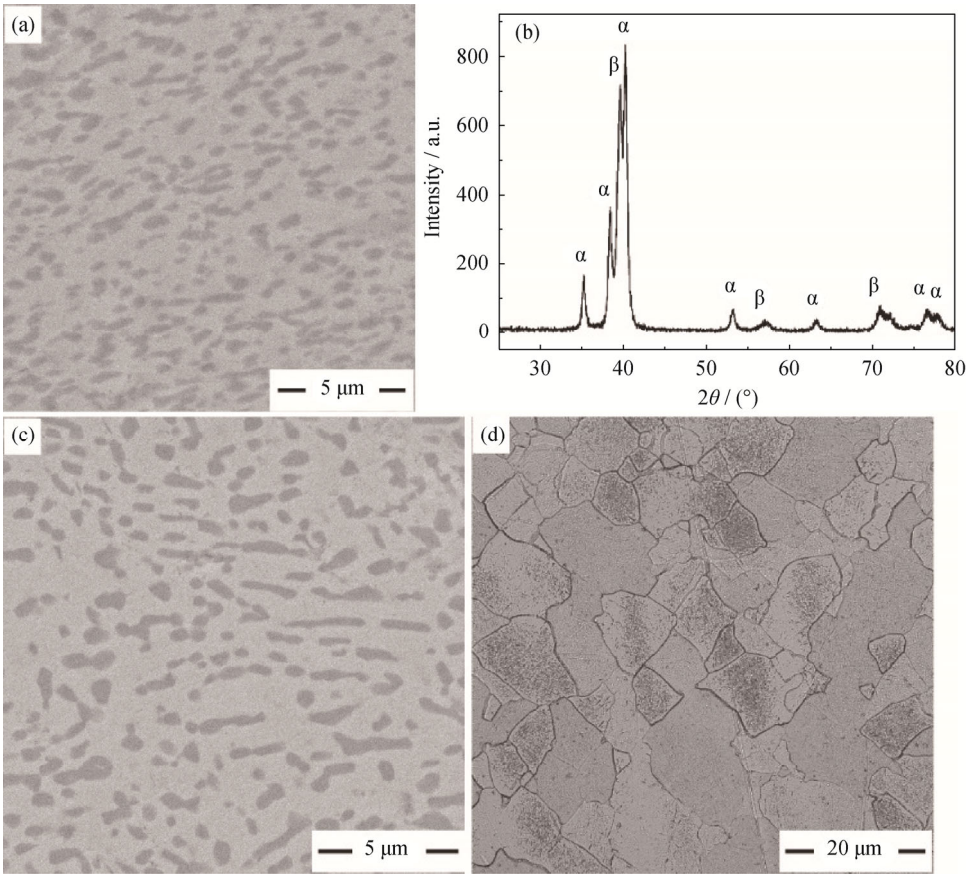

Fig. 10. As-forged Ti64–6Mo alloy: SEM image (a) and XRD pattern (b) of forged Ti64–6Mo alloy; SEM images of Ti64–6Mo alloy after solution treatment at 825 °C(c) and 900°C (d) for 0.5 h.

The effect of different aging temperatures on the microstructure of the alloy is shown in Fig. 11 for a solution temperature of 825°C. The microstructure of the alloy after aging consists of a primary spherical α phase and a needle-like

secondary α phase. When the alloy is aged at 520°C and 560°C, it exhibits a very fine secondary needle-like α-structure and the secondary α-structure has a large volume fraction. As the aging temperature increases to 600°C and 640°C, the fine secondary α phase gradually coarsens and the volume fraction decreases. Du *et al*. [37] pointed out that the higher aging temperature provides a larger growth drive force and a smaller nucleation driving force for the secondary α phase. Therefore, as the aging temperature increases, the secondary α phase is difficult to nucleate but grows easily, resulting in a thicker secondary α layer and a smaller volume fraction.

As shown in Fig. 12(a), when the alloy undergoes solution treatment in the two-phase region, the tensile strength decreases from 1464 MPa to 1233 MPa and the elongation of the alloy increases from 5.1% to 11.3% as the aging temperature increases from 520°C to 640°C. The stress–strain curve in Fig. 12(b) shows that the alloy exhibits enhanced plastic deformation resistance as the aging temperature increases.

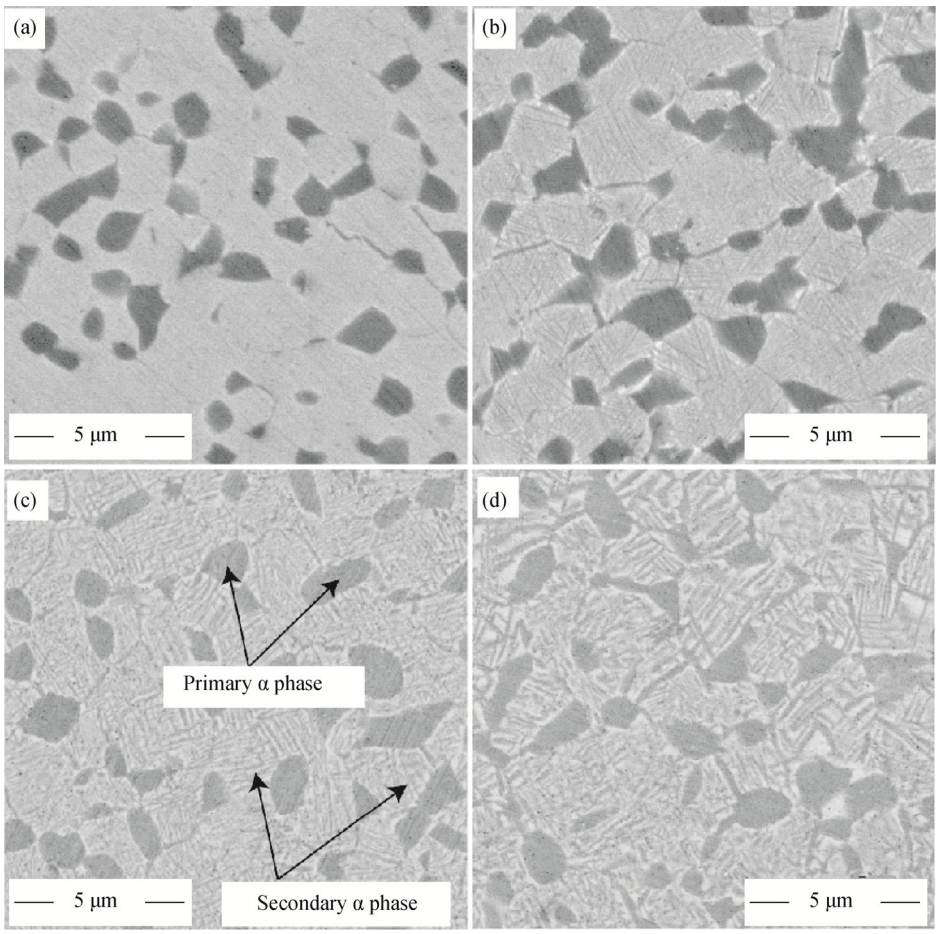

Fig. 11. SEM micrographs of the Ti64–6Mo alloy solution treated at 825°C and aged at 520°C (a), 560°C (b), 600°C (c), and 640°C (d) for 6 h.

When the solution temperature is 900°C (β single-phase region), the aged alloy is composed of a full needle-like structure, as shown in Fig. 13. As shown in Fig. 14, Thermo-Calc can be used to calculate the volume fraction of the secondary α phase; as the aging temperature increases, the volume fraction of the α phase gradually decreases and the needle-like α phase gradually coarsens. The β grains of the alloy solution treated in the β single-phase region are larger than that those of the alloy solution treated in the α+β two-phase region because of the absence of primary α phase, and the primary α phase can effectively hinder the grain boundary movement and inhibit the β grain growth. However, after solution treatment at 900°C (the single β-phase region), the size of the secondary α phase decreases. Because more α-phase stabilizing elements solve in the β phase and a larger precipitation driving force exists during the aging treatment, the nucleation rate after the solution treatment at 900°C is higher than that after the solution treatment (at 825°C). The change in the tensile properties of the alloy as a function of its aging temperature is shown in Fig. 12(c). The strength of the alloy decreases from 1572 to 1284 MPa as the aging temperature is increased from 520 to 640°C. The elongation increases from 2.6% to 6.5%.

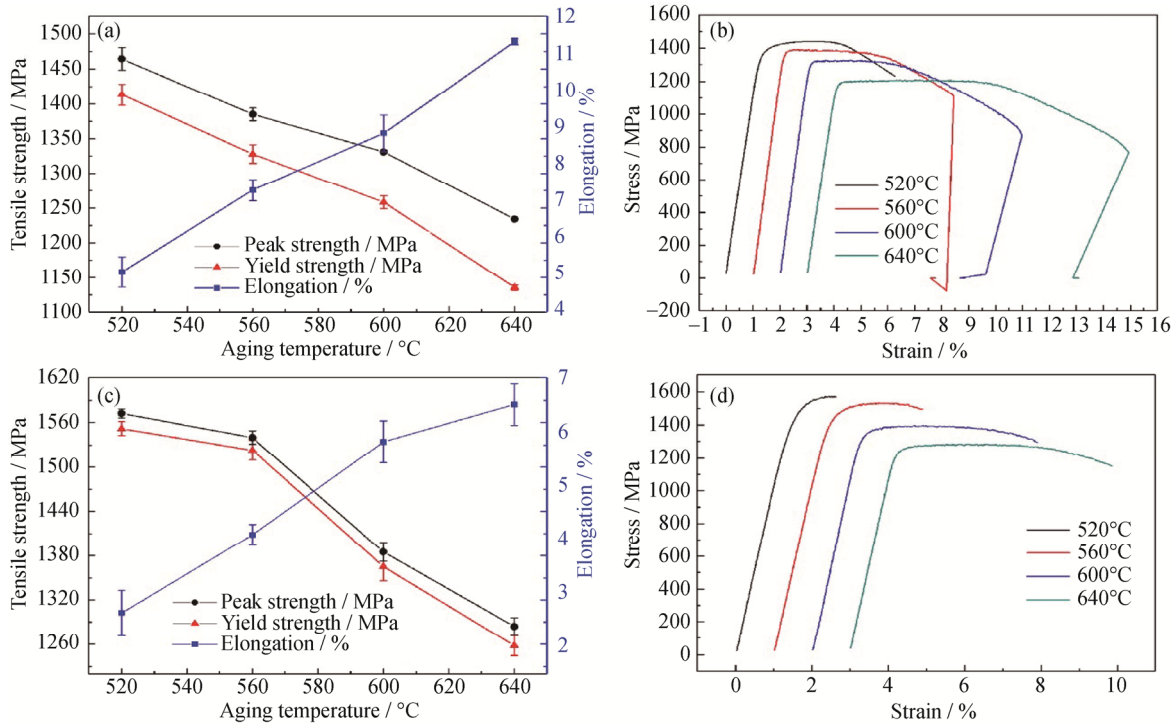

Fig. 12. Tensile properties of Ti64–6Mo alloy aged at different temperatures: (a, b) tensile properties after solution treatment at 825°C and the corresponding stress–strain curves; (c, d) tensile properties after solution treatment at 900°C and the corresponding stress–strain curves.

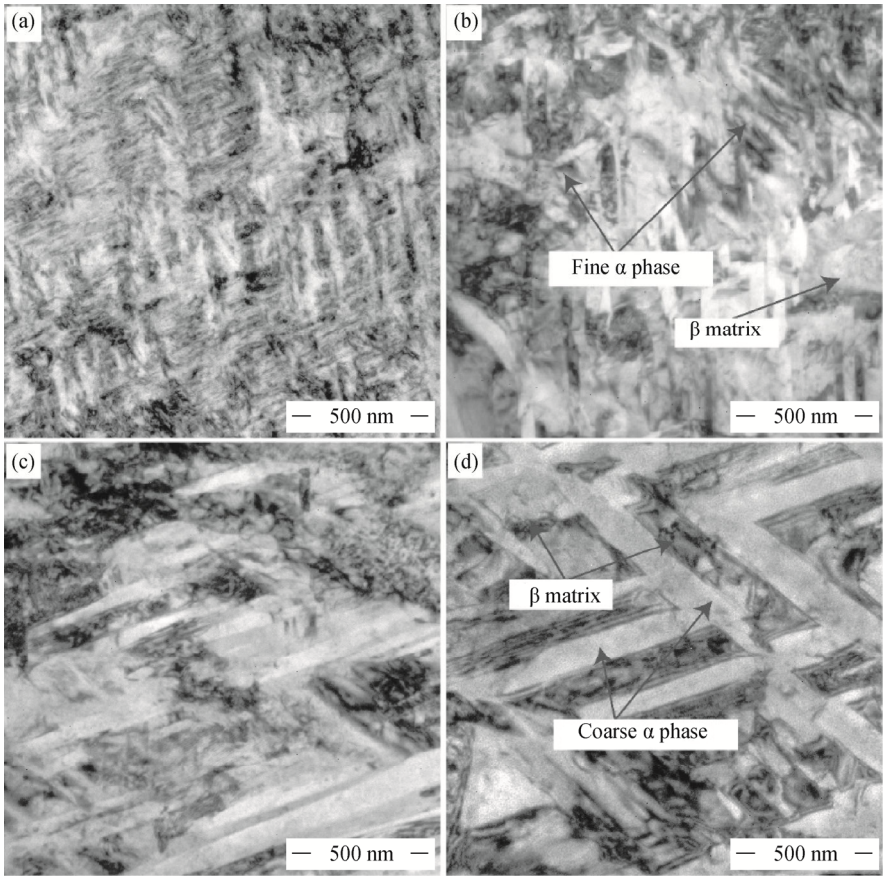

Fig. 13. SEM micrographs of the Ti64–6Mo alloy solution treated at 900°C and aged at 520°C (a), 560°C (b), 600°C (c), and 640°C (d) for 6 h.

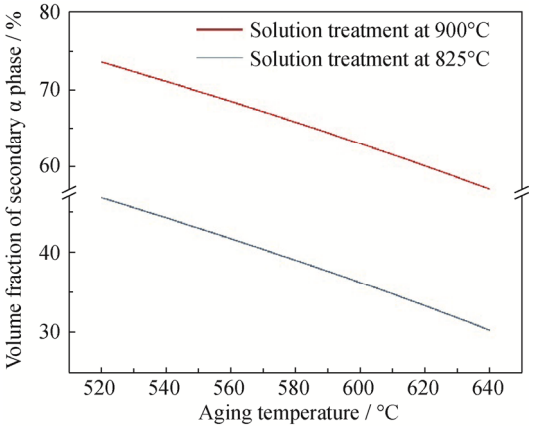

Fig. 14. The variation of the secondary α-phase volume fraction as a function of aging temperature, as calculated by Thermo-Calc.

4. Discussion

4.1. Microstructure of the Ti64−*x*Mo alloys

Fig. 5 shows that the change in the Mo content strongly influences the microstructure of the Ti64 alloy. When the Mo content is 0–5wt%, α′ martensite is formed by martensite transformation after quenching from the β single-phase region. During aging, the α′-to-α transition occurs upon diffusion of Mo, Al, and V atoms. Both the α′ and α phases have hcp structures; α is the stable phase, α′ is the metastable phase, and the α' phase is the supersaturated metastable α phase. In the Ti–Mo binary alloy [38], with increasing Mo content, the morphology of the α′ martensite gradually changes from massive to acicular and the α-phase morphology depends largely on the quenched α′ martensite. Therefore, when the Mo content is between 0 and 5wt%, the morphology of the α′ martensite and the α′ phase gradually changes from lath to needle.

When the alloy contains 6wt% Mo, the quenched Ti64–6Mo alloy presents a single bcc crystal structure and the β solution plus aged alloy exhibits a nanosized ultrafine α structure. Thus, the alloy has a very high nucleation rate in this phase-transformation process. No evidence of another metastable phase (such as ω and α″) was observed at this phase transformation, suggesting that the α phase forms directly with the hcp crystal structure. This phase transformation is an atypical homogeneous nucleation mechanism that does not utilize any heterogeneous nucleation sites. Recently, Ni and Khachaturyan [39] proposed the pseudo-spinodal mechanism. According to this mechanism, when the alloy composition is at the intersection ($c_0(T)$) of the Gibbs free-energy curve of the parent and generated phase, a slight fluctuation of composition will change the alloy composition of the local regions from the side where the free energy of the parent phase is lower than the generated phase to the side where the free energy of the parent phase is higher than that of the generated phase. In this local region, the generated phase has low energy and the parent phase will rapidly transform into the generated phase via a nondiffusion phase-transition mechanism to reduce the system energy, resulting in a high nucleation rate of the generated phase. In conjunction with the thermodynamic database for the Ti–Al–V–Mo system, the Thermo-Calc software was used to calculate the Gibbs free-energy curves for the α and β phases of Ti64–*x*Mo alloys at 600°C, as shown in Fig. 15. The results show that the intersection of the free-energy curves is just at the position where the alloy composition is Ti64–6Mo. Thus, the alloy composition is very close to the free-energy intersection point and small fluctuations in composition, as shown by the green arrow, may result in regions of the β-phase having compositions on the solute lean side of $c_0(T)$. These β regions will produce a driving force that transforms into α phase of the same composition (congruent transformation) to reduce the energy of the system (shown by the green arrow). The composition of the precipitated α phase, C_{init}, is derived from the fluctuation of the composition, far from reaching equilibrium C_{equil}. Continued heat treatment will be accompanied by the diffusion of alloying elements, and the compositions of the α and β phase would reach equilibrium. Thus, we can propose that the phase-transition mechanism during aging of the Ti64–6Mo at 600°C is a pseudo-spinodal mechanism.

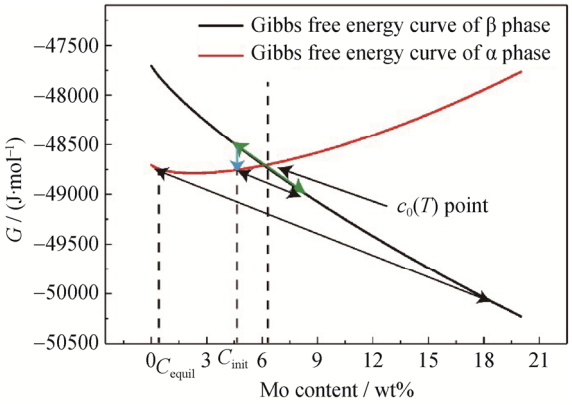

Fig. 15. Gibbs free-energy curves for α and β phases of Ti64−*x*Mo alloy at 600°C (the green arrow indicates component fluctuations; the blue arrow represents component fluctuations causing the α-phase free energy to be lower than the β-phase free-energy).

4.2. Hardness of Ti64−*x*Mo alloys

In the quenched state, the hardness of the Ti64–5Mo al-

loy is increased by ~100 MPa, reaching a peak of 508 MPa compared with that of the Ti64 alloy, which is attributable mainly to the contribution of the fine dispersion of α′ phase. This phenomenon indicates that the hardness of the alloy largely depends on the thickness of the quenched lath martensite. These diffusely distributed martensite structures form remarkable α′/β-phase interfaces in the β matrix, and these phase boundaries effectively hinder the slip of dislocations and increase the hardness of the alloy. When the Mo content increases from 5wt% to 7wt%, the amount of α′ decreases, the alloy structure becomes a single β phase, the strength decreases rapidly, and the hardness increases slowly with increasing Mo content because of solution strengthening. Wang *et al*. [32] and Oliveira *et al*. [40] also reported that Mo is a very effective solid-solution strengthener in Ti–Al–V–Mo alloys.

The microstructure and hardness of Ti64–*x*Mo alloys were analyzed in the aging state, and the grain boundary strengthening is the main strengthening mechanism, which means that the hardness of the alloy mainly depends on the α phase size. As shown in Figs. 6(b) and 7(b), the thickness of the α phase decreases from 1100 to 50 nm and the hardness of the alloy increases from 431 MPa to 597 MPa as the Mo content increases from 0 to 6wt%. With decreasing thickness of the α phase, the number of α/β grain boundaries in the alloy gradually increases. These grain boundaries can effectively hinder dislocation slip and increase the alloy strength. In addition, the volume fraction of the alpha phase also affects the alloy hardness. Kar *et al*. [41] have reported that, with a 55%–65% volume fraction of the α phase in the Ti-5553 alloy, the alloy attains its maximum strength when the volume fraction of the α phase in the Ti64–6Mo alloy is approximately 62%, which is one of the reasons why its hardness reaches a maximum. Wang *et al*. [42] have demonstrated the effective hardening effect of Mo in Ti–Al–V–Mo alloy. In this study, Ti64–6Mo alloy has the highest hardness and finest microstructure, together with an appropriate α-phase volume fraction in the series of Ti64–*x*Mo alloys. Thus, Ti64–6Mo alloy is a promising high-strength Ti alloy.

4.3. Tensile properties of Ti64–6Mo alloy

As shown in Fig. 12, as the aging temperature increases, the tensile strength of the alloy decreases, and the elongation increases. This phenomenon is mainly due to the microstructure and the strengthening mechanism of the Ti alloy. It indicated that secondary α phase which was precipitated in the aging stage acts as a strengthening phase and effectively hinders the dislocation slip. The lower aging temperature produces finer secondary α phase, resulting in numerous grain boundaries and strengthening of the alloy. The morphology of the primary and secondary α phases in Ti alloys plays a critical role in determining the properties of the alloy. The equation for yield strength can be expressed as [43]

$$\sigma = \text{function of } (f_{\alpha_p}/d_{\alpha_p} + f_{\alpha_s}/d_{\alpha_s}) \quad (1)$$

where σ is the yield strength, f_{α_p} is the primary α-phase volume fraction, d_{α_p} is the primary α-phase grain size, and α_p and α_s are the primary and secondary α phases, respectively. The strength of the alloy increases proportionally with the number density of the secondary and primary α phases. As the number of primary and secondary alpha phases increases, the yield strength of the alloy increases. The strength of the alloy is inversely proportional to the size of the primary and secondary alpha phases: as the size of the α phases decreases, the alloy strength increases.

The fact that the elongation of the alloy changes with the aging temperature is also related to the thickness and volume fraction of the secondary alpha phase in the alloy. Srinivasu *et al*. [44] found a large number of dislocations in the secondary α phase and the β matrix in the aged alloys. They also found that the plastic deformation process is the result of the coordinated deformation of α and β phases. During the tensile deformation of the alloy, the thin secondary α phase has a small space for plastic deformation, which leads to rapid deformation hardening, which in turn leads to the failure of the deformation of the α and β phase and results in a decrease in alloy plasticity. In addition, the deformability of the α phase (hcp structure) is weaker than that of the β phase (bcc structure), and a high volume fraction of the secondary α phase leads to a decrease in alloy plasticity.

When the aging temperature is determined, the strength of the alloy solution treated in the β-phase zone is higher than in the α + β-phase zone because the former has a finer and larger volume fraction of the secondary α phase than the latter. The law of variation of intensity can also be expressed using Eq. (1). Compared with the solution treatment in the α + β zone, the alloy plasticity after the solution treatment in the β-phase zone sharply decreases because of two effects. First, the single-phase zone solution treatment results in a large β grain size in the alloys. Second, the small grain size is likely to increase the alloy ductility because it can make the coordinated deformation between the grains easy and enhance the crack propagation resistance. In addition, Huang *et al*. [45] and Jackson *et al*. [46] demonstrated that the presence of the primary α phase can improve the ductility of the alloy.

The α + β-phase-zone solution-treated alloy consists of a

spherical primary α phase and a β matrix filled with needle-like secondary α phase. The primary α phase is the soft phase, and the β matrix filled with needle-like secondary α phase is the hard phase. Qin *et al*. [47] investigated the tensile deformation of Ti-5553 alloys, where planar slippage, deformation twinning, and dislocation tangling are observed in the primary α particle, indicating that the primary α phase had sufficient plastic deformation capacity that can coordinate deformation between the lamellar units and increase the ductility of the alloys. The β matrix, which is covered with needle-like secondary α phase, can only undergo twin deformation; its plastic deformation ability is much weaker than that of primary α phase. Therefore, samples solution treated in the single β-phase zone exhibit poor plasticity.

In this study, the diffusion-multiples approach was used to study the dependence of the change in Mo content on the microstructure and properties of Ti64 alloy, and Ti64–6Mo alloy was designed. The change in microstructure and properties of the Ti64 alloy with Mo content is similar to that of Ti–10Zr–*x*Mo alloy [48], which is investigated by a traditional metallurgy method. This approach shows that the experimental results of the diffusion multiple are reliable. Only one diffuse multiple sample was needed in this experiment; by contrast, for metallurgy methods, more than a dozen samples are required. This method has greatly improved the experimental efficiency and reduces cost.

5. Conclusions

In this work, the microstructure and properties of Ti64 alloy were studied with respect to their dependence of Mo content using high-throughput experimental methods, and a new high-strength Ti alloy, i.e., Ti64–6Mo, was designed. The quenched martensite gradually decreased and disappeared as the Mo content was increases to 6wt%. The fraction of the α phase of the aged alloy decreased to 62%, and the alloy obtained an ultrafine structure with high hardness. The α- and β-phase Gibbs free energy of the Ti64–*x*Mo alloy were calculated. The alloy composition is just located at the free-energy intersection point $c_0(T)$ of the free-energy curves of the α and β phases. The nucleation characteristics of the α phase are consistent with the pseudo-strip decomposition mechanism. The calculation results of phase composition and phase fraction of the α and β phases of the Ti64–*x*Mo alloy show good agreement with the experimental results. The Ti64–6Mo alloy subjected to a single-phase-zone solid-solution and aging treatment exhibits high strength and poor plasticity. A high strength and moderate plasticity can be obtained via an α/β two-phase-region solution treatment plus aging. The tensile properties are dependent on the size of the β grains and the size and fraction of the secondary and primary α phases.

Acknowledgements

The authors acknowledge financial support from the National Key Technologies R&D Program of China (Grant No. 2016YFB0701301 and 2018YFB0704100), National Natural Science Foundation of China (Grant No. 51671218 and 51501229), National Key Basic Research Program of China (973 Program) (Grant No. 2014CB644000) and State Key Laboratory of Powder Metallurgy, Central South University, Changsha, China.

References

[1] H.X. Li, X.Y. Nie, Z.B. He, K.N. Zhao, Q. Du, J.S. Zhang, and L.Z. Zhuang, Interfacial microstructure and mechanical properties of Ti–6Al–4V/Al7050 joints fabricated using the insert molding method, *Int. J. Miner. Metall. Mater.*, 24(2017), No. 12, p. 1412.

[2] M.K. Ibrahim, E. Hamzah, S.N. Saud, E.N.E. Abu Bakar, and A. Bahador, Microwave sintering effects on the microstructure and mechanical properties of Ti–51at% Ni shape memory alloys, *Int. J. Miner. Metall. Mater.*, 24(2017), No. 3, p. 280.

[3] R.R. Boyer, An overview on the use of titanium in the aerospace industry, *Mater. Sci. Eng. A*, 213(1996), No. 1-2, p. 103.

[4] T.N. Prasanthi, C. Sudha, and S. Saroja, Effect of alloying elements on interdiffusion phenomena in explosive clads of 304LSS/Ti–5Ta–2Nb alloy, *J. Mater. Sci.*, 51(2016), No. 11, p. 5290.

[5] H.P. Duan, H.X. Xu, W.H. Su, Y.B. Ke, Z.Q. Liu, and H.H. Song, Effect of oxygen on the microstructure and mechanical properties of Ti–23Nb–0.7Ta–2Zr alloy, *Int. J. Miner. Metall. Mater.*, 19(2012), No. 12, p. 1128.

[6] S.L. Semiatin, P.N. Fagin, M.G. Glavicic, I.M. Sukonnik, and O.M. Ivasishin, Influence on texture on beta grain growth during continuous annealing of Ti–6Al–4V, *Mater. Sci. Eng. A*, 299(2001), No. 1-2, p. 225.

[7] Y.J. Lai, S.W. Xin, P.X. Zhang, Y.Q. Zhao, F.J. Ma, X.H. Liu, and Y. Feng, Recrystallization behavior of Ti40 burn-resistant titanium alloy during hot working process, *Int. J. Miner. Metall. Mater.*, 23(2016), No. 5, p 581.

[8] T. Seshacharyulu, S.C. Medeiros, J.T. Morgan, J.C. Malas, W.G. Frazier, and Y.V.R.K. Prasad, Hot deformation and microstructural damage mechanisms in extra-low interstitial (ELI) grade Ti–6Al–4V, *Mater. Sci. Eng. A*, 279(2000), No. 1-2, p. 289.

[9] A. Nocivin, I. Cinca, D. Raducanu, V.D. Cojocaru, and I.A. Popovici, Mechanical properties of a Gum-type Ti–Nb–Zr–Fe–O

alloy, *Int. J. Miner. Metall. Mater.*, 24(2017), No. 8, p. 909.
[10] S. Raghunathan, R.J. Dashwood, M. Jackson, S.C. Vogel, and D. Dye, The evolution of microtexture and macrotexture during subtransus forging of Ti–10V–2Fe–3Al, *Mater. Sci. Eng. A*, 488(2008), No. 1-2, p. 8.
[11] G.T. Terlinde, T.W. Duerig, and J.C. Williams, Microstructure, tensile deformation, and fracture in aged ti 10V–2Fe–3Al, *Metall. Trans. A*, 14(1983), No. 10, p. 2101.
[12] B. He, X.J. Tian, X. Cheng, J. Li, and H.M. Wang, Effect of weld repair on microstructure and mechanical properties of laser additive manufactured Ti-55511 alloy, *Mater. Des.*, 119(2017), p. 437.
[13] S. Nag, R. Banerjee, J.Y. Hwang, M. Harper, and H.L. Fraser, Elemental partitioning between α and β phases in the Ti–5Al–5Mo–5V–3Cr–0.5Fe (Ti-5553) alloy, *Philos. Mag.*, 89(2009), No. 6, p. 535.
[14] F.W. Chen, G.L. Xu, X.Y. Zhang, K.C. Zhou, and Y.W. Cui, Effect of α morphology on the diffusional β↔α transformation in Ti-55531 during continuous heating: Dissection by dilatometer test, microstructure observation and calculation, *J. Alloys Compd.*, 702(2017), No. 25, p. 352.
[15] J.K. Fan, J.S. Li, H.C. Kou, K. Hua, and B. Tang, The interrelationship of fracture toughness and microstructure in a new near β titanium alloy Ti–7Mo–3Nb–3Cr–3Al, *Mater. Charact.*, 96(2014), p. 93.
[16] B. Cherukuri, R. Srinivasan, S. Tamirisakandala, and D.B. Miracle, The influence of trace boron addition on grain growth kinetics of the beta phase in the beta titanium alloy Ti–15Mo–2.6Nb–3Al–0.2Si, *Scripta Mater.*, 60(2009), No. 7, p. 496.
[17] N.G. Jones, R.J. Dashwood, M. Jackson, and D. Dye, Development of chevron-shaped α precipitates in Ti–5Al–5Mo–5V–3Cr, *Scripta Mater.*, 60(2009), No. 7, p. 571.
[18] A. Dehghan-Manshadi and R.J. Dippenaar, Development of α-phase morphologies during low temperature isothermal heat treatment of a Ti–5Al–5Mo–5V–3Cr alloy, *Mater. Sci. Eng. A*, 528(2011), No. 3, p 1833.
[19] J.K. Fan, H.C. Kou, M.J. Lai, B. Tang, H. Chang, and J.S. Li, Characterization of hot deformation behavior of a new near beta titanium alloy: Ti-7333, *Mater. Des.*, 49(2013), p. 945.
[20] J.I. Qazi, H.J. Rack, and B. Marquardt, High-strength metastable beta-titanium alloys for biomedical applications, *JOM*, 56(2004), No. 11, p. 49.
[21] R. Banerjee, S. Nag, J. Stechschulte, and H.L. Fraser, Strengthening mechanisms in Ti–Nb–Zr–Ta and Ti–Mo–Zr–Fe orthopaedic alloys, *Biomaterials*, 25(2004), No. 17, p. 3413.
[22] T. Zhou, M. Aindow, S.P. Alpay, M.J. Blackburn, and M.H. Wu, Pseudo-elastic deformation behavior in a Ti/Mo-based alloy, *Scripta Mater.*, 50(2004), No. 3, p. 343.
[23] T. Oyama, C. Watanabe, and R. Monzen, Growth kinetics of ellipsoidal ω-precipitates in a Ti–20 wt%Mo alloy under compressive stress, *J. Mater. Sci.*, 51(2016), No. 19, p. 8880.
[24] C.H. Wang, C.D. Yang, M. Liu, X. Li, P.F. Hu, A.M. Russell, and G.H. Cao, Martensitic microstructures and mechanical properties of as-quenched metastable β-type Ti–Mo alloys, *J. Mater. Sci.*, 51(2016), No. 14, p. 6886.
[25] R. Monzen, R. Kawai, T. Oyama, and C. Watanabe, Tensile-stress-induced growth of ellipsoidal ω-precipitates in a Ti–20wt%Mo Alloy, *J. Mater. Sci.*, 51(2016), No. 5, p. 2490.
[26] J.C. Zhao, A combinatorial approach for efficient mapping of phase diagrams and properties, *J. Mater. Res.*, 16(2001), No. 6, p. 1565.
[27] J.C. Zhao, X. Zheng, and D.G. Cahill, High-throughput diffusion multiples, *Mater. Today*, 8(2005), No. 10, p. 28.
[28] J.C. Zhao, X. Zheng, and D.G. Cahill, High-throughput measurements of materials properties, *JOM*, 63(2011), No. 3, p. 40.
[29] X. Zheng, D.G. Cahill, P. Krasnochtchekov, R.S. Averback, and J.C. Zhao, High-throughput thermal conductivity measurements of nickel solid solutions and the applicability of the Wiedemann-Franz law, *Acta Mater.*, 55(2007), No. 15, p. 5177.
[30] X.D. Zhang, L.B. Liu, J.C. Zhao, J.L. Wang, F. Zheng, and Z.P. Jin, High-efficiency combinatorial approach as an effective tool for accelerating metallic biomaterials research and discovery, *Mater. Sci. Eng. C*, 39(2014), No. 1, p. 273.
[31] D. Wu, L.B. Liu, L.G. Zhang, L.J. Zeng, and X. Shi, Investigation of the influence of Cr on the microstructure and properties of Ti6Al4V*x*Cr alloys with a combinatorial approach, *J. Mater. Eng. Perform.*, 26(2017), No. 9, p. 4364.
[32] C. Wang, N. Li, Y. Cui, and M.T. Pérez-Prado, Effect of solutes on the rate sensitivity in Ti–*x*Al–*y*Mo–*z*V and Ti–*x*Al–*y*Mo–*z*Cr β–Ti alloys, *Scripta Mater.*, 149(2018), p. 129.
[33] J.C. Williams and B.S. Hickman, Tempering behavior of orthorhombic martensite in titanium alloys, *Metall. Mater. Trans. B*, 1(1970), No. 9, p. 2648.
[34] H.Y. Kim, Y. Ikehara, J.I. Kim, H. Hosoda, and S. Miyazaki, Martensitic transformation, shape memory effect and superelasticity of Ti–Nb binary alloys, *Acta Mater.*, 54(2006), No. 9, p. 2419.
[35] W.F. Ho, S.C. Wu, S.K. Hsu, Y.C. Li, and H.C. Hsu, Effects of molybdenum content on the structure and mechanical properties of as-cast Ti–10Zr-based alloys for biomedical applications, *Mater. Sci. Eng. C*, 32(2012), No. 3, p. 517.
[36] W.F. Ho, S.C. Wu, H.H. Chang, and H.C. Hsu, Structure and mechanical properties of Ti–5Cr based alloy with Mo addition, *Mater. Sci. Eng. C*, 30(2010), No. 6, p. 904.
[37] Z. Du, S. Xiao, L. Xu, J. Tian, F. Kong, and Y. Chen, Effect of heat treatment on microstructure and mechanical properties of a new β high strength titanium alloy, *Mater. Des.*, 55(2014), No. 55, p. 183.
[38] W.F. Ho, C.P. Ju, and J.H. Lin, Structure and properties of cast binary Ti–Mo alloys, *Biomaterials*, 20(1999), No. 22, p. 2115.
[39] Y. Ni and A.G. Khachaturyan, From chessboard tweed to chessboard nanowire structure during pseudospinodal decomposition, *Nat. Mater.*, 8(2009), No. 5, p. 410.
[40] N.T.C. Oliveira and A.C. Guastaldi, Electrochemical stability

and corrosion resistance of Ti–Mo alloys for biomedical applications, *Acta Biomater.*, 5(2009), No. 1, p. 399.

[41] S.K. Kar, A. Ghosh, N. Fulzele, and A. Bhattacharjee, Quantitative microstructural characterization of a near beta Ti alloy, Ti-5553 under different processing conditions, *Mater. Charact.*, 81(2013), No. 4, p. 37.

[42] C.Y. Wang, L.W. Yang, Y.W. Cui, and M.T. Pérez-Prado, High throughput analysis of solute effects on the mechanical behavior and slip activity of beta titanium alloys, *Mater. Des.*, 137(2017), p. 371.

[43] L. Mora, C. Quesne, C. Haut, C. Servant, and R. Penelle, Relationships among thermomechanical treatments, microstructure, and tensile properties of a near beta-titanium alloy: β-CEZ: Part I. relationships between thermomechanical treatments and microstructure, *J. Mater. Res.*, 11(1996), No. 1, p. 89.

[44] G. Srinivasu, Y. Natraj, A. Bhattacharjee, T.K. Nandy, and G.V.S.N. Rao, Tensile and fracture toughness of high strength β titanium alloy, Ti–10V–2Fe–3Al, as a function of rolling and solution treatment temperatures, *Mater. Des.*, 47(2013), p. 323.

[45] J. Huang, Z. Wang, and K. Xue, Cyclic deformation response and micromechanisms of Ti alloy Ti–5Al–5V–5Mo–3Cr–0.5Fe, *Mater. Sci. Eng. A*, 528(2011), No. 29-30, p. 8723.

[46] M. Jackson, N.G. Jones, D. Dye, and R.J. Dashwood, Effect of initial microstructure on plastic flow behaviour during isothermal forging of Ti–10V–2Fe–3Al, *Mater. Sci. Eng. A*, 501(2009), No. 1-2, p. 248.

[47] D. Qin, Y. Lu, D. Guo, L. Zheng, Q. Liu, and L. Zhou, Tensile deformation and fracture of Ti–5Al–5V–5Mo–3Cr–1.5Zr–0.5Fe alloy at room temperature, *Mater. Sci. Eng. A*, 587(2013), p. 100.

[48] W.F. Ho, S.C. Wu, S.K. Hsu, Y.C. Li, and H.C. Hsu, Effects of molybdenum content on the structure and mechanical properties of as-cast Ti–10Zr-based alloys for biomedical applications, *Mater. Sci. Eng. C*, 32(2012), No. 3, p. 517.